AIAA SciTech Forum
January 3-7, 2022, San Diego, CA & Virtual
AIAA SCITECH 2022 Forum

10.2514/6.2022-1787

Wind Turbine Efficiency Enhancement by CoFlow Jet Airfoil

Yan Ren * Kewei Xu † Gecheng Zha ‡
Coral Gables, FL 33124
Dept. of Mechanical and Aerospace Engineering
University of Miami, Coral Gables, Florida 33124

Abstract

The aerodynamic performance and flow structures of a high efficiency Co-Flow Jet (CFJ) wind turbine is studied in this paper. CFJ is a zero-net-mass-flux active flow control method that dramatically increases airfoil lift coefficient and suppresses flow separation at a low energy expenditure. The 3D Reynolds Averaged Navier-Stokes (RANS) equations with one-equation Spalart-Allmaras (SA) turbulence model are solved to simulate the 3D flows of the wind turbines. The CFJ-Wind Turbine in this paper utilizes a new CFJ-NACA6421 airfoil, but the twist and chord distributions are the same as those of the NREL 5.029m radius Phase VI wind turbine, which is used as the baseline turbine for comparison. The predicted power coefficient of the baseline turbine agrees excellently with the measured one by a small deviation of 1.1%. The predicted surface pressure distributions are also in very good agreement with the experiment. The CFJ injection and suction slots are implemented along the blade span to achieve CFJ active flow control. The study indicates that the CFJ active flow control can significantly enhance the power output of a well optimized conventional wind turbine at its design flow speed. The results show that the flow field around the CFJ wind turbine blade surface suppressed flow separation near the blade root region. The parametric study show that the optimum jet momentum coefficient C_μ is 0.02. At the same design RPM of the baseline blade with a tip speed ratio of 5.4 and freestream speed of 7 m/s, the CFJ turbine achieves a power coefficient of 0.475, a 29.4% improvement over the baseline turbine's design point efficiency. At a higher RPM with the tip speed ratio of 6.3, the CFJ wind turbine net power coefficient is 0.492, which presents 34.1% improvement comparing to the NREL Phase VI wind turbine at its design point. The work on more parametric study is in progress to further optimize the design.

Nomenclature

CFJ	Co-flow jet
U	Flow Velocity
ρ	Air Density
α, AoA	Angle of Attack
$\dot{m}$	Mass Flow Rate
M	Mach Number
Re	Reynolds Number
L	Aerodynamics Lift
D	Aerodynamic Drag

* Postdoc Researcher, Ph.D., AIAA member
† Postdoc Researcher, Ph.D.
‡ Professor, AIAA Associate Fellow, Professor of the University of Miami

p	Static Pressure
p_0	Total Pressure
η	Pumping Power
C_M	Moment Coefficient, $\frac{M}{q_\infty S c}$
C_p	Pressure Coefficient, $\frac{p-p_\infty}{q_\infty}$
C_μ	Jet Momentum Coefficient, $\frac{\dot{m}_j v_j}{q_\infty S}$
P_c	Co-Flow Jet power coefficient
P_w	Turbine rotor output power
C_{pr}	Turbine rotor power coefficient
C_{pw}	Turbine net power coefficient
∞	Free Stream Conditions

1 Introduction

Wind energy is the fastest growing energy sector due to its sustainability, renewability and low emission. Therefore, wind turbines, the machinery to extract wind energy, have been widely studied. The most important aerodynamic measure of merit of wind turbines is their power output, not at the high speed greater than the rated speed, but at the speed lower than the rated speed. When the speed is very high, the power output of a wind turbine needs to be limited to avoid the failure of the wind turbine structure and the electric generator system. At low speed, the structure limit is not an issue and it is desirable to increase the power. Typically, a turbine is designed to have an optimum efficiency at a certain ratio of the tip speed to the freestream flow speed. When the freestream velocity is greater or smaller than that, the efficiency will drop and may be compensated by varying its pitch angle or rotational speed. At a low speed, the way to increase the power output is to increase the aerodynamic lift coefficient and the ratio of lift to drag by increasing the angle of attack (AoA). However, the AoA is limited to avoid blade stall and its dynamic loads. Within a one-year cycle, wind turbines work most of the time at the speed lower than their rated speed (e.g. 70-80%). Thus increasing the power output of wind turbines at low speed is essential to increase its power capacity factor.

The other important issue for wind turbine aerodynamic design is to minimize the dynamic loading due to flow separation for long life span. One cause of wind turbine dynamic loads is the randomness nature of wind. During operation, wind direction and velocity magnitude vary constantly, which alternates flows between being separated and attached on wind turbine blades. The other cause of wind turbine dynamic loads is mostly related to the downwind turbine. When a turbine blade passes the tower wake of a downwind turbine, the blade will experience a large angle of attack swing, which usually create blade dynamic stall [1]. Due to the hysteresis effect of dynamic stall, the lift and drag could experience violent oscillation that produce the dynamic load for the blade. The dynamic loads limit the power output and may exert extreme loading on the wind turbines, reducing wind turbine lifespan. The wind turbine gear boxes and blades are usually most vulnerable to dynamic loads. Downwind turbines have advantages of lower mass and manufacturing cost, particularly suitable for offshore floating turbines[2]. But the tower wake dynamic loads must be mitigated. To increase wind turbine power output and mitigate flow fluctuation, passive and active flow control methods have been attempted for wind turbine blades [3]. However, the benefit from the past flow controls is very limited due to the complexity, low effectiveness, and cost. However, active flow control is the path for potential large improvement of wind turbine energy output [3, 4].

The recently developed Co-flow Jet (CFJ) flow control is a zero-net-mass-flux (ZNMF) active flow control that is able to dramatically enhance the airfoil performance [5, 6, 7, 8, 9, 10, 11]. As shown in Fig. 1, a CFJ airfoil

withdraws a small amount of mass flow from trailing edge, pressurizes it by the a series of low pressure fans, and injects the flow at leading edge tangential to the mainstream. It is demonstrated numerically and experimentally that CFJ achieves radical lift augmentation, drag reduction and stall angle of attack increase [5, 6, 7, 8, 9, 10, 11]. Lefebvre and Zha[12] implement CFJ on a pitching airfoil and basically remove its hysteresis.

Xu and Zha in 2021 [13] apply CFJ to S809 wind turbine airfoil and achieved an optimal configuration of CFJ-S809 airfoil with significant improvement of C_L and aerodynamic efficiency (C_L/C_D). Xu and Zha [14] further numerically applied CFJ-S809 airfoil to the NREL Phase IV 10 m diameter horizontal axis wind turbine and validated the simulation with the test results [15]. The baseline NREL turbine achieved peak efficiency of 41% at the speed of 7m/s and its optimum pitch angle of 3°. At this pitch angle, the CFJ airfoil hardly increased the efficiency. However, when the pitch angle was intentionally reduced by 13° (AoA increased by 13°), the baseline turbine stalls with negative power output, whereas the CFWJ wind turbine had no flow separation and increased the power output by 20.3% with an efficiency of 51% . This example shows the new design strategy that takes advantage of CFJ airfoil with an AoA limit higher than conventional design. For wind turbine applications, the HVAC fans or similar system could be used as the CFJ actuators for their required low pressure ratio and high mass flow rate [13, 14].

A novel aerodynamic design method that can increase the lift coefficient and the ratio of lift to drag without stalling the blade is appealing. This is the motivation of the present study. The purpose of this paper is to continue exploring the benefit of the Coflow Jet wind turbine blades by employing an advanced 21% thickness CFJ airfoil, which is different from the widely used S809 airfoil. The same NREL Phase VI 10.06m diameter horizontal axis wind turbine [15] is used as the reference for comparison.

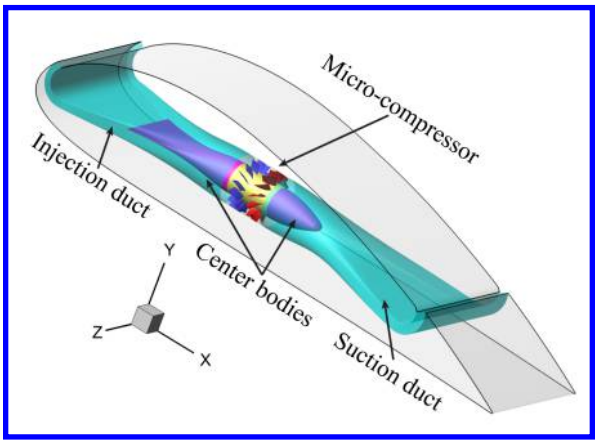

Figure 1: Schematics of the CFJ airfoil with embedded micro-compressor

2 Aerodynamic Forces and Power

The velocity determining the aerodynamic force acting on a wind turbine blade at a radius R is the relative velocity, also called apparent wind velocity as labled in Fig. 2. The airfoil will generate a lift and drag as illustrated in Fig. 2. The tangential force rotates the blades and generates power output.

The tangential force at radius R can be expressed as:

$$dF_t = dL\cos(\alpha) - dD\sin(\alpha) = n(0.5\rho V_{rel}^2)C_L[\cos(\alpha) - \frac{1}{C_L/C_D}\sin(\alpha)]cdR \tag{1}$$

where L stands for the lift, D for the drag, V_{rel} is the relative velocity at radius R, α is the angle between the relative velocity and the turbine axis as shown in Fig. 2, C_L and C_D are the airfoil lift and drag coefficient, c is the airfoil chord at radius R, and n is the number of blades.

The total power output of a wind turbine is the torque multiplied by angular velocity. Based on Eq. (1), the power coefficent is calculated as:

$$C_{pr} = \frac{n}{\pi} \int_{\bar{R}_{root}}^{\bar{R}_{tip}} \bar{\rho} \bar{V}_{rel}^2 C_L [\cos(\alpha) - \frac{1}{C_L/C_D} \sin(\alpha)] \bar{c} \overline{\omega R} d\bar{R} \tag{2}$$

where ω is the angular velocity of the blades. All the variables with overhead bar stand for normalized variables as: $\bar{R} = R/R_{tip}$, $\bar{\rho} = \rho/\rho_\infty$, $\bar{V}_{rel} = V_{rel}/V_\infty$, and $\overline{\omega R} = \omega R/V_\infty$.

The flow angle α, which is determined by the ratio of the incoming wind speed and blade rotating speed, is also important to determine the optimum power coefficient as shown in Eq. (2). The wind turbine research community in general adopts the ratio of the blade tip speed to wind speed in the range of 7 to 10[16], which then determines the α distribution along the blade. A turbine blade is usually twisted to have the optimum angle of attack along the span.

Eq. (2) indicates that both a high lift coefficient and a high C_L/C_D are beneficial to increase the power coefficient. Usually, the angle of attack(AoA) for maximum C_L/C_D is faily low such as about 3° to 5°. The maximum C_L would occur near stall and the AoA is high and should be avoided. Typical wind turbines select the design AoA to favor maximum C_L/C_D to have enough stall margin. Thumthae and Chitsomboon suggest that the optimum AoA should be between the one for maximum C_L/C_D and maximum C_L[17]. Huyer et al indicate that wind turbines must be designed to achieve the maximum efficiency at or near the static stall AoA since the AoA of dynamic stall is usually higher than the static stall AoA [1]. The CFJ wind turbines are aimed at dramatically increasing C_L and C_L/C_D, and at the smae time using minimal energy expenditure to achieve net power output gain.

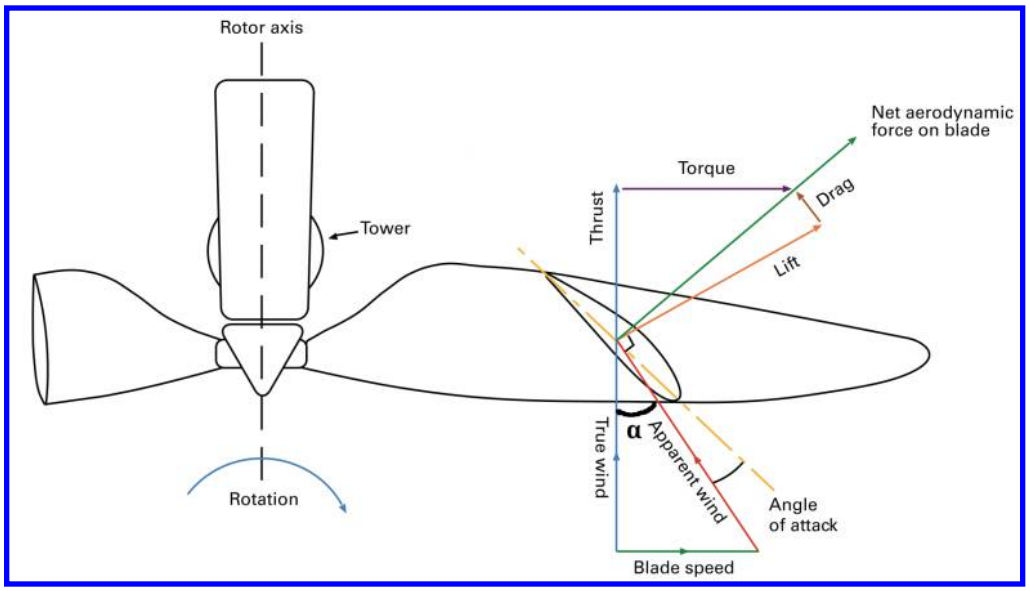

Figure 2: Aerodynamic forces acting on a wind turbine airfoil at a certain radius(plot modified from [18]).

3 The Co-Flow Jet Wind Turbine Parameters

To facilitate the description of CFJ wind turbine performance, several important parameters are given below.

3.1 Jet Momentum Coefficient

The injection jet momentum coefficient C_μ is used to describe the CFJ strength as:

$$C_\mu = \frac{\dot{m}V_j}{\frac{1}{2}\rho_\infty {U_\infty}^2 A_{ref}} \tag{3}$$

where $\dot{m}$ is the injection mass flow, V_j is the mass-averaged injection relative velocity, ρ_∞ denotes the free stream density, and A_{ref} is the reference area defined as the disk area of the wind turbine, U_∞ is the freestream velocity.

3.2 Co-Flow Jet Power Coefficient

The CFJ power required is determined by the total enthalpy rise in the turbine rotating frame from the suction duct outlet to the injection duct inlet [19, 14]. The total enthalpy rise can be achieved by the embedded fans. The power required by the CFJ can be expressed as:

$$P = \frac{\dot{m}H_{t2}}{\eta}(\Gamma^{\frac{\gamma-1}{\gamma}} - 1) \tag{4}$$

where, $\dot{m}$ is the CFJ mass flow rate, H_{t2} is the total enthalpy in the turbine rotating frame at the suction slot, Γ is the total pressure ratio in the turbine rotating frame between the injection and suction, and η is the pumping system efficiency. For the CFJ wind turbine, the $\dot{m}$, H_{t2} and Γ are calculated in the rotational frame of reference using relative properties.

Eq. (4) indicates that the power required by the CFJ is linearly determined by the mass flow rate and exponentially by the total pressure ratio. This relationship in fact applies to all the active flow controls based on fluidic actuators. The power coefficient is defined as:

$$P_c = \frac{P}{\frac{1}{2}\rho_\infty U_\infty^3 A_{ref}} \tag{5}$$

where P is the CFJ required power defined in Eq. (4).

3.3 CFJ Wind Turbine Net Power Coefficient

The wind turbine net power coefficient C_{pw} is commonly used to designate the efficiency of the entire turbine power system. For a conventional wind turbine, the C_{pw} is defined as:

$$C_{pw} = C_{pr} = \frac{P_w}{\frac{1}{2}\rho_\infty U_\infty^3 A_{ref}} \tag{6}$$

where P_w is the wind turbine rotor output power, C_{pr} is wind turbine rotor power coefficient. The C_{pw} and C_{pr} are the same for conventional wind turbine. For the CFJ wind turbine, the net power coefficient C_{pw} is defined as:

$$C_{pw} = C_{pr} - P_c \tag{7}$$

where P_c is the CFJ power coefficient defined in Eqn. 7.

4 Governing Equations

The governing equations are the Navier-Stokes equations in rotating frame with the effects of Coriolis force ($2\omega \times \mathbf{V}$) and centrifugal force ($\omega \times \omega \times \mathbf{r}$). The normalized Reynolds Averaged Navier-Stokes governing equations with SpalartAllmaras one-equation turbulent model [20] in generalized coordinates are given by:

$$\frac{\partial \mathbf{Q}}{\partial t} + \frac{\partial \mathbf{E}}{\partial \xi} + \frac{\partial \mathbf{F}}{\partial \eta} + \frac{\partial \mathbf{G}}{\partial \zeta} = \frac{1}{Re}\left[\frac{\partial \mathbf{R}}{\partial \xi} + \frac{\partial \mathbf{S}}{\partial \eta} + \frac{\partial \mathbf{T}}{\partial \zeta}\right] + \mathbf{D} \tag{8}$$

where Re is the Reynolds number. The conservative variable vector $\mathbf{Q}$, invisid flux $\mathbf{E}$, viscous flux vector $\mathbf{R}$ and source term $\mathbf{D}$ are expressed as follows, and the rest can be expressed following the symmetric rule.

$$\mathbf{Q} = \frac{1}{J}\begin{bmatrix} \rho \\ \rho u \\ \rho v \\ \rho w \\ \rho e \\ \rho \hat{\nu} \end{bmatrix} \tag{9}$$

$$\mathbf{E} = \frac{1}{J}\begin{bmatrix} \rho U \\ \rho u U + p\xi_x \\ \rho v U + p\xi_y \\ \rho w U + p\xi_z \\ (\rho e + p)U \\ \rho \hat{\nu} U \end{bmatrix} \tag{10}$$

$$\mathbf{R} = \frac{1}{J}\begin{bmatrix} 0 \\ \tau_{xi}\xi_i \\ \tau_{yi}\xi_i \\ \tau_{zi}\xi_i \\ (u_j\tau_{ij} - q_i)\xi_i \\ \frac{\rho}{\sigma}(\nu + \hat{\nu})\frac{\partial \hat{\nu}}{\partial x_i}\xi_i \end{bmatrix} \tag{11}$$

$$\mathbf{D} = \frac{1}{J}\begin{bmatrix} 0 \\ 0 \\ \rho {R_0}^2 y + 2\rho R_0 w \\ \rho {R_0}^2 z - 2\rho R_0 v \\ 0 \\ S_\nu \end{bmatrix} \tag{12}$$

where R_0 is the Rossby number defined as $(\omega L_\infty)/U_\infty$. ω is the angular velocity of the rotor rotation, L_∞ is the reference length and U_∞ is the freestream velocity. The normalized equation of state as a constitutve equation relating density to pressure and temperature is expressed in the rotating frame as

$$\rho e = \frac{p}{\gamma - 1} + \frac{1}{2}\rho(u^2 + v^2 + w^2) - \frac{1}{2}\rho r^2 {R_0}^2 \tag{13}$$

The S_ν in Eq. (14) is the source term for the S-A model,

$$\begin{aligned} S_\nu = \rho c_{b1}\left(1 - f_{t2}\right)\tilde{S}\tilde{\nu} + \tfrac{1}{Re}\Big[-\rho\left(c_{w1} f_w - \tfrac{c_{b1}}{\kappa^2} f_{t2}\right)\left(\tfrac{\tilde{\nu}}{d}\right)^2 \\ + \tfrac{\rho}{\sigma} c_{b2}\left(\nabla\tilde{\nu}\right)^2 - \tfrac{1}{\sigma}\left(\nu + \tilde{\nu}\right)\nabla\tilde{\nu} \bullet \nabla\rho\Big] + Re\left[\rho f_{t1}\left(\Delta q\right)^2\right] \end{aligned} \tag{14}$$

Other auxiliary relations and coefficients for the S-A turbulence model can be found in [20, 21].

5 Numerical Methods

The in-house high order accuracy CFD code Flow-Acoustics-Structure Interaction Package (FASIP) is used to conduct the numerical simulation. The 3D Reynolds Averaged Navier-Stokes (RANS) equations with one-equation Spalart-Allmaras [20] turbulence model described above are solved. A 3rd order MUSCL scheme for the inviscid flux [22, 23, 24] and a 2nd order central differencing for the viscous terms are employed to discretize the Navier-Stokes equations. The low diffusion Roe flux difference scheme is used to evaluate the inviscid fluxes. Implicit time marching method using Gauss-Seidel line relaxation is used to achieve a fast convergence rate [25]. Parallel computing is implemented to save wall clock simulation time [26]. The FASIP code is intensively validated for CFJ flow control simulations [6, 7, 8, 27, 28, 29, 30, 31, 32, 33], turbomachinery multistage flows[34, 35], and wind turbines [14].

As shown in Fig. 3, the computational domain consists of a rotational inner domain (in blue) and a stationary outer domain (in black). The rotational domain is 0.6R in x direction, 2.6R in y direction, and 1.3R in z direction. The stationary domain is 12.6R in x directoin, 26.7R in y direction, and 13.3R in z direction. Frozen rotor boundary condition is applied on the interface between rotational and stationary domains with the blade located at zero azimuth. The mesh at the rotational frame and stationary frame are one-to-one connected to ensure flux conservation. The flow variables are converted between the rotational and stationary frames. The boundary conditions of total pressure, total temperature and flow angle are imposed at the upstream inlet boundary of the stationary domain. A static pressure boundary condition is applied at the outlet boundary. Only one blade is simulated with the 180° periodic boundary condition applied on two sides of the hub domain. The convergence criterion is that the L2-norm residual reduced by more than 4 orders of magnitude.

The computational domain shown in Fig. 3 is meshed using structured grid with an overall mesh size of 10 million points. The mesh size and number of points in each direction are similar to those used by other research

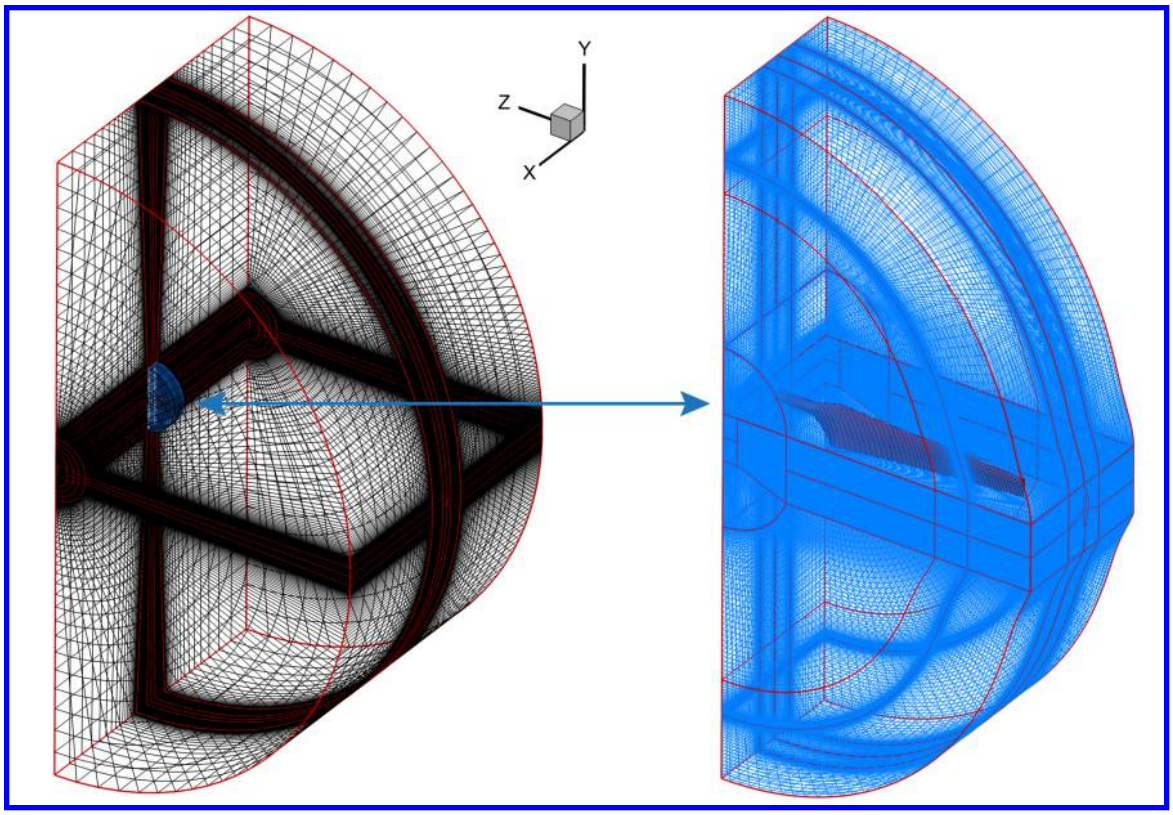

Figure 3: Mesh topology

groups in [36, 37]. The first grid cell spacing normalized by the airfoil chord at mid-span (0.5m) close to blade wall is set to 1×10^{-5} to ensure y^+ close to 1.

6 Results

In this section, the validation results of the baseline S809 NREL phase VI rotor are presented first. All simulations are conducted at the freestream speed $U_\infty = 7m/s$,which is the design speed that the turbine achieves the optimal efficiency. The results are compared with published wind tunnel experimental results to validate our in-house flow solver. The simulation results of the CFJ wind turbine (Fig. 4), which uses an optimized CFJ-NACA6421 airfoil, are presented next. The effect of jet momentum coefficient C_μ and wind turbine RPM are investigated. The corresponding case parameters are listed in table 1. The CFJ-NACA6421 airfoil has 21% thickness, 16.7% thicker than the S809 airfoil. The corresponding chord and twist distributions are kept the same as those of the Phase VI wind turbine rotor designed by National Renewable Energy Laboratory (NREL) [15].

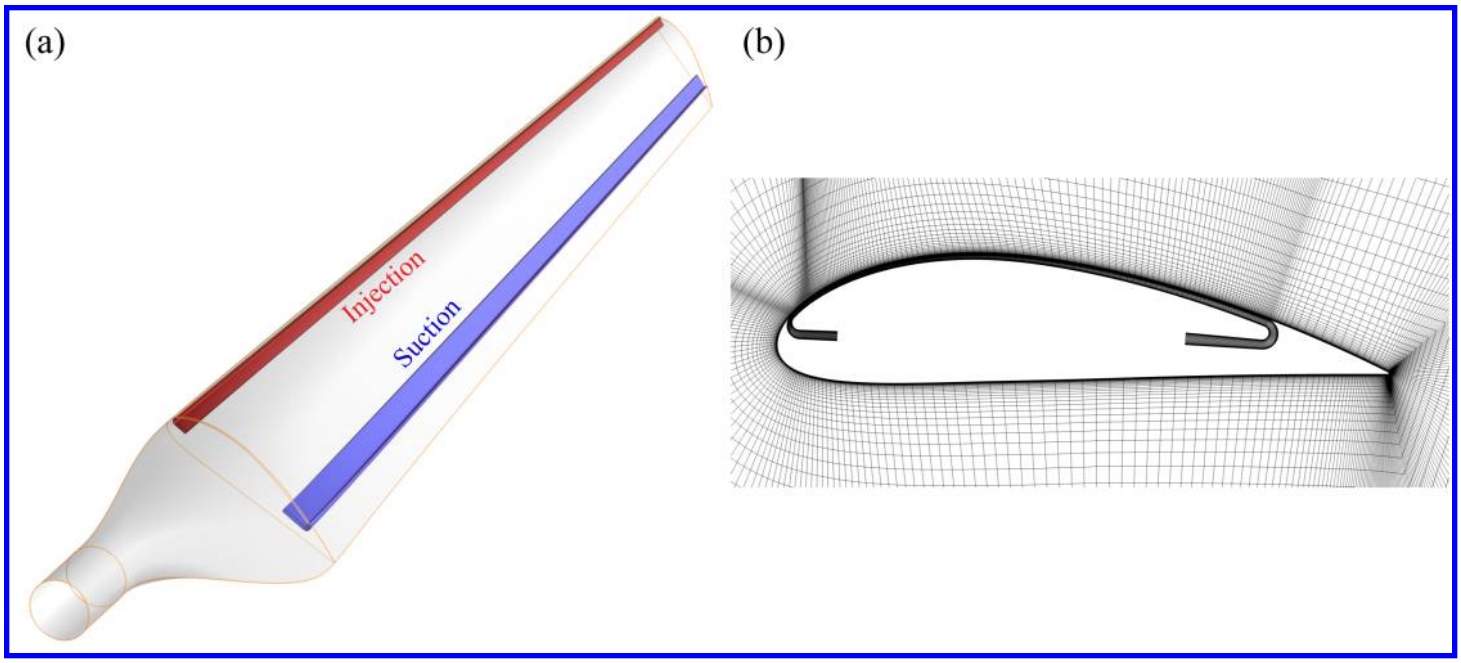

Figure 4: (a) Geometry of the CFJ-Wind Turbine; (b) CFJ-NACA6421 airfoil with 2D computational mesh

Table 1: Simulation parameters used in the current work.

Cases	U_∞	Pitch	C_μ	RPM
BL: Baseline NREL S809	7m/s	3°	N/A	72
C1, C2, C3, C4			0.01, 0.02, 0.03, 0.04	60
C5, C6, C7, C8			0.01, 0.02, 0.03, 0.04	72
C9, C10, C11, C12			0.01, 0.02, 0.03, 0.04	84

6.1 The Baseline (BL) NREL Phase VI Rotor Validation

Experimental and CFD simulation results of the Phase VI wind turbine rotor from the NREL [15] are presented in this section for validation. The wind turbine has two blades and is 5.029 meter in radius (R). It stacked using S809 airfoil along the span. More details regarding blade geometry and wind tunnel testing can be found in [15]. Table 2 shows the performance comparison of the experiment and the CFD simulation. The CFD prediction is excellent and the difference of the wind turbine power coefficients between experiment and CFD is 1.1%.

Table 2: Performance comparison of experiment and simulation.

Cases	U_∞	Pitch	RPM	Shaft Torque	C_{pw}
Expt.: S809 NREL phase VI	7m/s	3°	72	800.78Nm	0.363
BL: Baseline NREL S809				809.69Nm	0.367

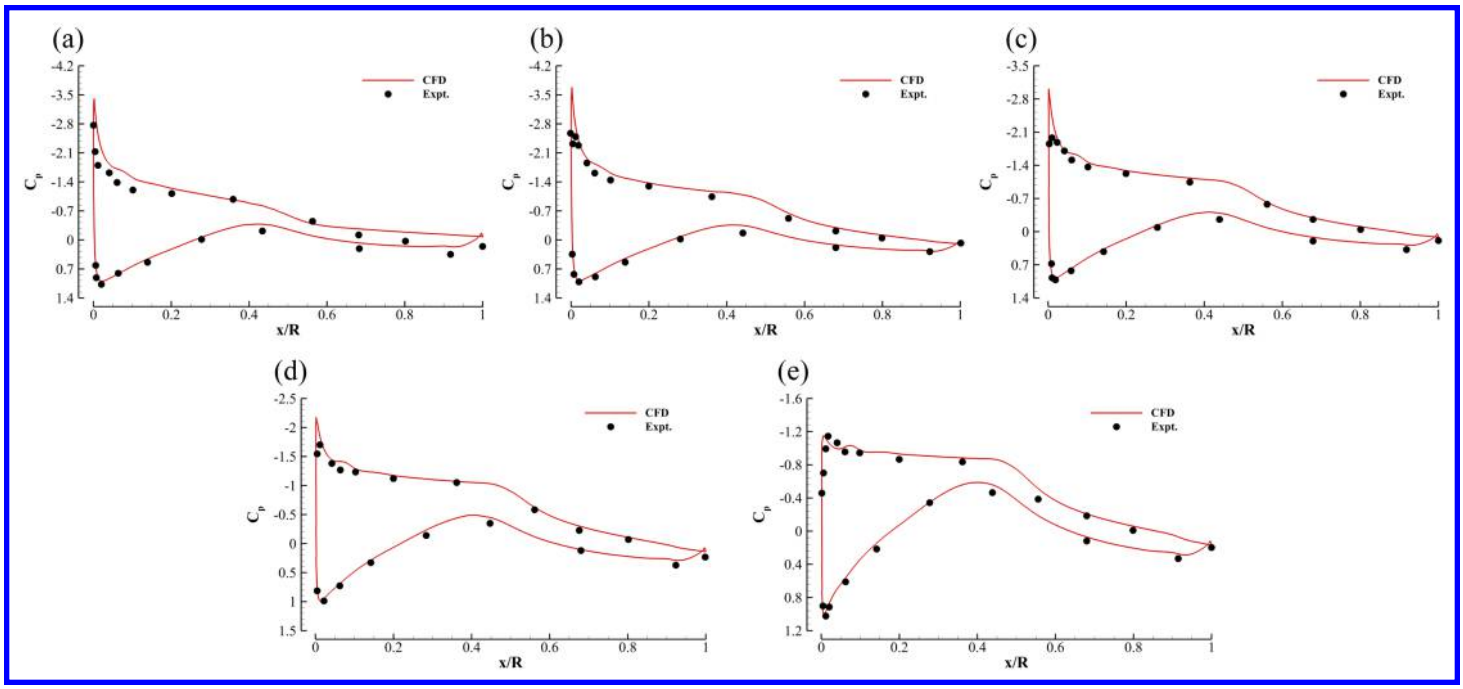

Figure 5: C_p distributions of the NREL phase VI wind turbine at wind speed of 7m/s, pitch angle of 3°. (a) 30% span; (b) 46.7% span; (c) 63.3% span; (d) 80% span; (e) 95% span.

Fig. 5 shows the C_p comparison between the CFD prediction and the experiment at five span locations. We can see that the agreement is very good. Overall, The power and C_p predicted by the present numerical simulation achieves a very good agreement with the experiment and is thus used as reference to compare the performance of the CFJ wind turbine.

6.2 The Co-Flow Jet Wind Turbine with CFJ-NACA6421 airfoil

The aerodynamic performance and flow structures of the CFJ wind turbine with CFJ-NACA6421 airfoil are presented in this section. The same airfoil twist along the span and the same pitch angle of 3° are used.

Fig. 6 shows the CFJ wind turbine performance at different C_μ and rotor RPM. The rotor power coefficient C_{pr} increases with the rise of C_μ, and so does the CFJ power coefficient P_c. The CFJ wind turbine net power coefficient C_{pw} reaches maximum value at $C_\mu = 0.02$ for all RPM. In addition, all the power coefficients increase with the rise of rotor RPM. At the same RPM as that of the baseline turbine with the tip speed ratio of 5.4, the CFJ turbine Case C6 achieves a power coefficient of 0.475, a 29.4% improvement. Since all the twist and pitching conditions are the same, this benefit is purely from the CFJ effect. The best C_{pw} in the current study is 0.492 occurring at the RPM of 84, 16.7% higher than the baseline RPM. This achieves a power coefficient improvement of 34.1%, another 5% improvement due to the more favored tip speed ratio of 6.3. These results show that the wind turbine efficiency is significantly improved with the help of the CFJ active flow control technology.

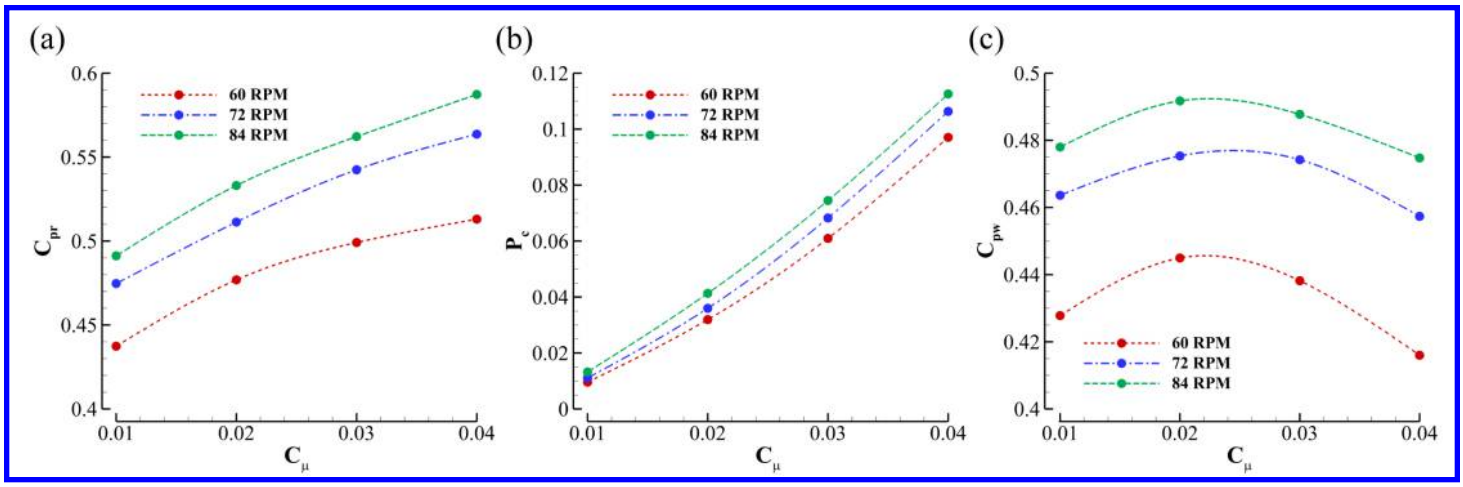

Figure 6: CFJ wind turbine performance at different C_μ and rotor RPM. (a) Rotor power coefficient; (b) CFJ power coefficient; (c) wind turbine net power coefficient.

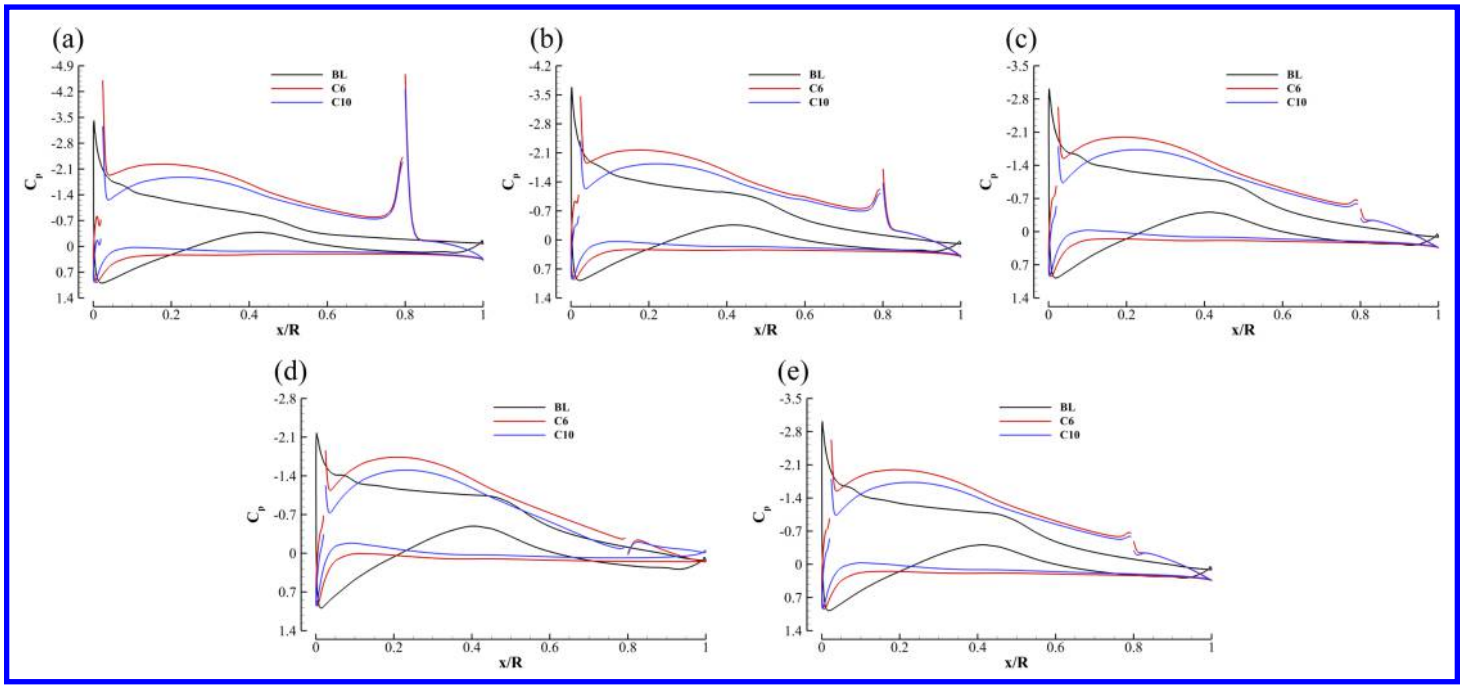

Figure 7: C_p distribution of the case BL, C6, and C10 at wind speed of 7m/s, pitch angle of 3°. (a) 30% span; (b) 46.7% span; (c) 63.3% span; (d) 80% span; (e) 95% span.

Fig. 7 shows the C_p comparison of the case BL, C6, and C10. The discontinuities on the C_p distributions of CFJ wind turbines are due to the CFJ injection and suction slots. It is clear from the C_p plots that the surface loading is increased for the case C6 and C10 mostly in the rear part of the CFJ-NACA6421 airfoil due to avoiding the rapidly reduced thickness of S809 airfoil, and the power generation due to the lift is thus also increased as the result. The CFJ active flow control substantially decrease the surface pressure on the turbine blade suction surface and increase the pressure on the pressure surface. By observing the C_p curves opening size at leading edge in Fig. 7, we can see that both the CFJ case has smaller angle of incidence (angle between incoming flow direction and the mean line of the airfoil) than the baseline case. This appears to be attributed to the larger leading radius

of NACA6421 airfoil. The blade loading for the C10 case is actually smaller than the C6 case due to lower AoA at higher RPM. The C10 case has higher power coefficient benefited from the higher RPM that generates high relative velocity as shown in Eq. 2. The results indicate that there is still potential to further increase the power coefficient of case C10 by reducing the pitch angle to generate higher AoA. The surface pressure on the turbine blade pressure surface increased near the mid chord region.

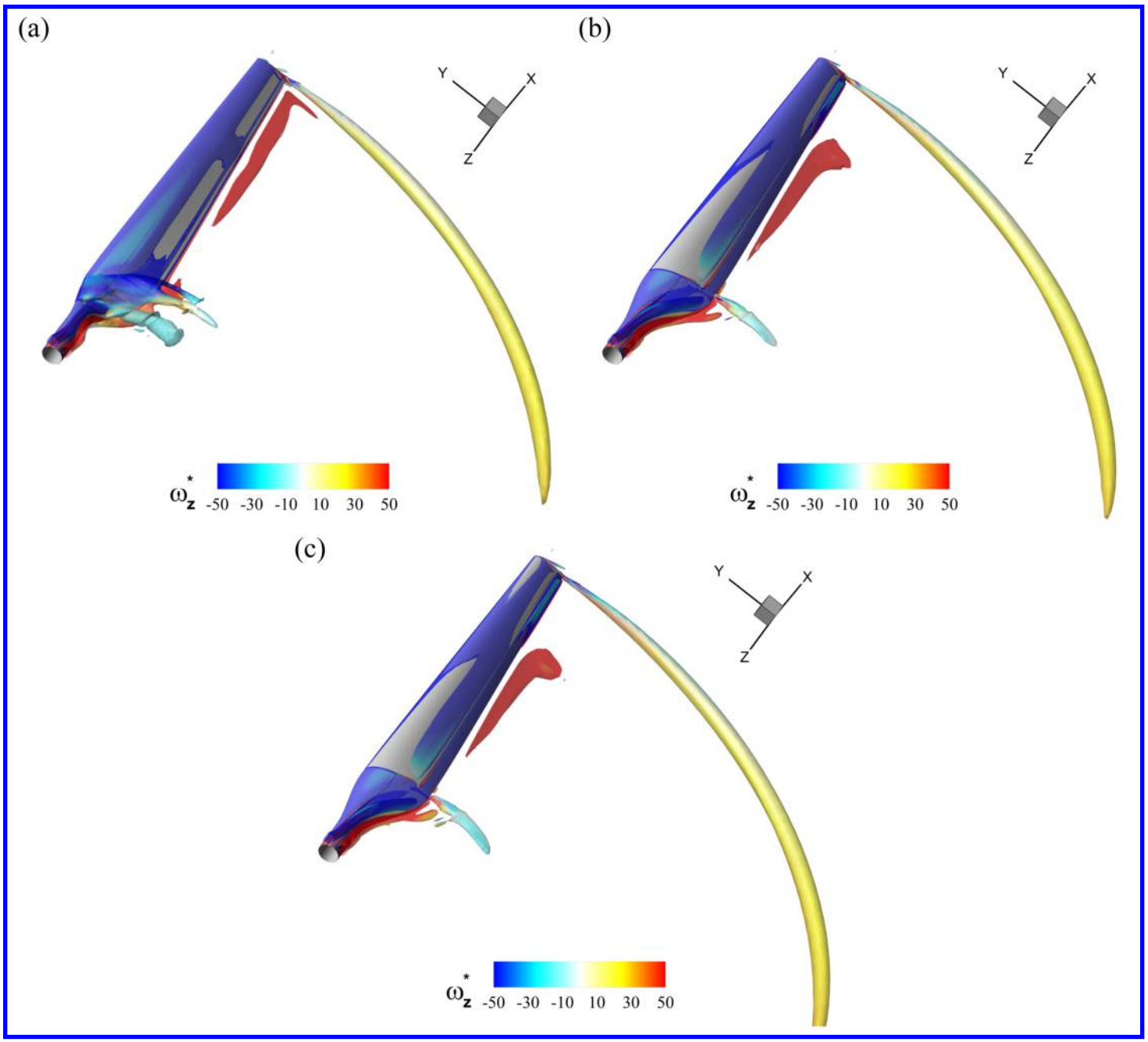

Figure 8: Iso-surface of Q-criterion around wind turbine rotor blade showing vortical structures, colored by normalized z-direction vorticity ω_z^*. (a) Case BL; (b) case C6; (c) case C10.

Fig. 8 shows the 3D vortical structures around the wind turbine. The BL case and two best performance CFJ

wind turbine cases (C6 and C10) are discussed here. Case C6 has the same rotation speed (72 RPM) as the case BL. Case C10 has larger rotation speed (84 RPM) and best wind turbine net power coefficient of all cases studied in the present work. As shown in Fig. 8, all three cases show good flow attachment except for the part near the rotor blade root of the case BL. A slender blade tip vortex tube can be observed for all three cases and the tip vortex is longer for case C10 since it has larger blade rotation speed. Flow separation near the blade root is suppressed with the CFJ active flow control.

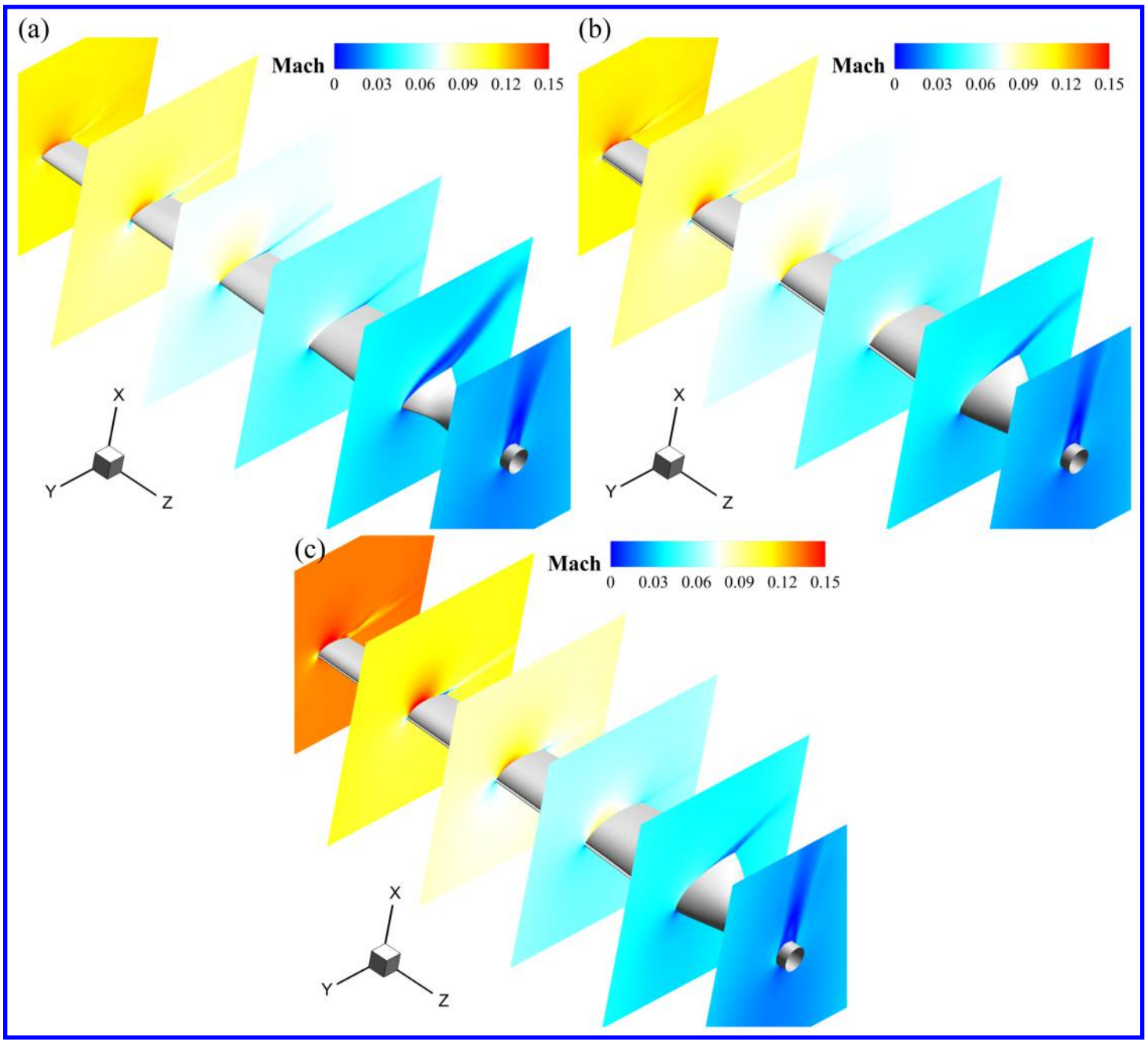

Figure 9: Flow slices along the wind turbine span (2%, 21.4%, 40.8%, 60.2% 79.6%, 99% span). Mach contours in rotational frame are shown. (a) Case BL; (b) case C6; (c) case C10.

Fig. 9 shows flow slices of Mach contours along the wind turbine span for the case BL, case C6, and case C10. The Mach contours in rotational frame are shown at those slices. For the case BL, tiny low speed region can be observed at 40.8%, 60.2%, and 79.6% span, while large flow separation can be identified at 2% and 21.4% span (blade root region). For the case C6, which has the same blade rotation speed as the case BL, the low speed region at 40.8%, 60.2%, and 79.6% span disappeared, and the flow separation at 2% and 21.4% span become much smaller. In addition, high speed regions at the blade leading edge become larger for the case C6.

For the case C10, which has larger blade rotation speed and presents the best wind turbine net power coefficient, the high speed regions at the blade leading edge become even larger comparing to the case C6. The flow separation near the blade root is further reduced comparing to the case C6. Eq. 2 indicates that at a certain range of the speed, a higher relative speed will generate more power.

7 Conclusion

The aerodynamic performance and flow structures of a high efficiency Co-Flow Jet (CFJ) wind turbine is studied in this paper. The 3D Reynolds Averaged Navier-Stokes (RANS) equations with one-equation Spalart-Allmaras (SA) turbulence model are solved to simulate the 3D flows of the wind turbines. The CFJ-Wind Turbine in this paper utilizes a new CFJ-NACA6421 airfoil, but the twist and chord distributions are the same as those of the NREL 5.029m radius Phase VI wind turbine, which is used as the baseline turbine for comparison. The predicted power coefficient of the baseline turbine agrees excellently with the measured one by a small deviation of 1.1%. The predicted surface pressure distributions are also in very good agreement with the experiment. The CFJ injection and suction slots are implemented along the blade span to achieve CFJ active flow control. The study indicates that the CFJ active flow control can significantly enhance the power output of a well optimized conventional wind turbine at its design flow speed. The results show that the flow field around the CFJ wind turbine blade surface suppressed flow separation near the blade root region. The parametric study show that the optimum jet momentum coefficient C_μ is 0.02. At the same design RPM of the baseline blade with a tip speed ratio of 5.4 and freestream speed of 7 m/s, the CFJ turbine achieves a power coefficient of 0.475, a 29.4% improvement over the baseline turbine's design point efficiency. At a higher RPM with the tip speed ratio of 6.3, the CFJ wind turbine net power coefficient is 0.492, which presents 34.1% improvement comparing to the NREL Phase VI wind turbine at its design point. The work on more parametric study is in progress to further optimize the design.

Disclosure: The University of Miami and Dr. Gecheng Zha may receive royalties for future commercialization of the intellectual property used in this study. The University of Miami is also equity owner in CoFlow Jet, LLC, licensee of the intellectual property used in this study.

References

[1] S. A. Huyer, D. Simms, and M. C. Robinson, "Unsteady aerodynamics associated with a horizontal-axis wind turbine," *AIAA journal*, vol. 34, no. 7, pp. 1410–1419, 1996.

[2] J. Koh and E. Ng, "Downwind offshore wind turbines: Opportunities, trends and technical challenges," *Renewable and Sustainable Energy Reviews*, vol. 54, pp. 797–808, 2016.

[3] C. Van Dam, D. E. Berg, and S. J. Johnson, "Active load control techniques for wind turbines.," tech. rep., Sandia National Laboratories, 2008.

[4] N. Johnson, P. Bortolotti, K. L. Dykes, G. E. Barter, P. J. Moriarty, W. S. Carron, F. F. Wendt, P. S. Veers, J. Paquette, C. Kelly, *et al.*, "Investigation of innovative rotor concepts for the big adaptive rotor project," tech. rep., National Renewable Energy Lab.(NREL), Golden, CO (United States), 2019.

[5] G.-C. Zha, B. F Carroll, C. D. Paxton, C. A. Conley, and A. Wells, "High-performance airfoil using coflow jet flow control," *AIAA journal*, vol. 45, no. 8, pp. 2087–2090, 2007.

[6] A. Lefebvre, B. Dano, W. Bartow, M. Fronzo, and G. Zha, "Performance and energy expenditure of coflow jet airfoil with variation of mach number," *Journal of Aircraft*, vol. 53, no. 6, pp. 1757–1767, 2016.

[7] G. Zha, W. Gao, and C.D. Paxton, "Jet Effects on Co-Flow Jet Airfoil Performance," *AIAA Journal*, vol. 45, pp. 1222–1231, 2007.

[8] G.-C. Zha, C. Paxton, A. Conley, A. Wells, nd B. Carroll, "Effect of Injection Slot Size on High Performance Co-Flow Jet Airfoil," *AIAA Journal of Aircraft*, vol. 43, pp. 987–995, 2006.

[9] Yang, Yunchao and Zha, Gecheng, "Super-Lift Coefficient of Active Flow Control Airfoil: What is the Limit?," *AIAA SCITECH2017, 55th AIAA Aerospace Science Meeting, Grapevine, Texas*, AIAA 2017-1693.

[10] J. Zhang, K. Xu, Y. Yang, Y. Ren, P. Patel, and G. Zha, "Aircraft control surfaces using co-flow jet active flow control airfoil." AIAA Paper 2018-3067, 2018 Applied Aerodynamics Conference, Atlanta, Georgia, June 25-29, 2018.

[11] K. Xu, J. Zhang, and G. Zha, "Drag minimization of co-flow jet control surfaces at cruise conditions." AIAA 2019-1848, AIAA Scitech 2019 Forum, San Diego, California, 7-11 January 2019.

[12] A. Lefebvre and G. Zha, "Numerical simulation of pitching airfoil performance enhancement using co-flow jet flow control," vol. 2517, 2013.

[13] K. Xu and G. Zha, "Investigation of coflow jet active flow control for wind turbine airfoil." AIAA Paper will be virtually presented in 2020 AIAA AVIATION Forum and Exposition, AIAA 2020-2942, 15-19 June, 2020.

[14] K.-W. Xu and G.-C. Zha, "High efficiency wind turbine using co-flow jet active flow control." ASME Paper GT2021-59664, Proceedings of ASME Turbo Expo 2021 Turbomachinery Technical Conference and Exposition, Virtual, Online, June 07-11, 2021.

[15] D. Simms, S. Schreck, M. Hand, and L. J. Fingersh, "NREL unsteady aerodynamics experiment in the NASA-Ames wind tunnel: a comparison of predictions to measurements," tech. rep., National Renewable Energy Lab., Golden, CO (US), 2001.

[16] Burton, T. and Jenkins, N. and Sharpe, D. and Bossanyi, E., "Wind Energy Handbook, 2nd Edition." ISBN: 978-0-470-69975-1, Wiley, June 2011.

[17] Thumthae, C. and Chitsomboon, T., " Optimal angle of attack for untwisted blade wind turbine," *Renewable Energy*, vol. 34, pp. 1279–1284, 2009.

[18] J. Manwell, J. McGowan, and A. Rogers, *Wind Energy Explained Theory, Design and Application.* ISBNs: 0-471-49972-2: John Wiley & Sons Ltd, 2002.

[19] Lefebvre, A. and Dano, B. and Bartow, W. and Di Franzo, M. and Zha, G.-C., "Performance and Energy Expenditure of Coflow Jet Airfoil with Variation of Mach Number." AIAA Paper 2013-0490, AIAA Journal of Aircraft, DOI: 10.2514/1.C033113, 2016.

[20] P. Spalart and S. Allmaras, "A One-equation Turbulence Model for Aerodynamic Flows." AIAA-92-0439, 30th Aerospace Sciences Meeting and Exhibit, Reno,NV,U.S.A., 06 January 1992 - 09 January 1992.

[21] B.-Y. Wang, B. Haddoukessouni, J. Levy, and G.-C. Zha, "Numerical Investigations of Injection Slot Size Effect on the Performance of Co-Flow Jet Airfoil." AIAA Paper 2007-4427, 2007.

[22] Y.-Q. Shen, G.-C. Zha, and B.-Y. Wang, "Improvement of Stability and Accuracy of Implicit WENO Scheme ," *AIAA Journal*, vol. 47, pp. 331–344, 2009.

[23] Shen, Y.-Q. and Zha, G.-C. and Chen, X.-Y., " High Order Conservative Differencing for Viscous Terms and the Application to Vortex-Induced Vibration Flows," *Journal of Computational Physics*, vol. 228(2), pp. 8283–8300, 2009.

[24] Shen, Y.-Q. and Zha, G.-C. , " Improvement of the WENO Scheme Smoothness Estimator," *International Journal for Numerical Methods in Fluids*, vol. DOI:10.1002/fld.2186, 2009.

[25] G.-C. Zha and E. Bilgen, "Numerical study of three-dimensional flows using unfactored upwind-relaxation sweeping algorithm," *Journal of Computational Physics*, vol. 125, no. 2, pp. 425–433, 1996.

[26] B. Wang, Z. Hu, and G.-C. Zha, "General subdomain boundary mapping procedure for structured grid implicit cfd parallel computation," *Journal of Aerospace Computing, Information, and Communication*, vol. 5, no. 11, pp. 425–447, 2008.

[27] B. Wang, B. Haddoukessouni, J. Levy, and G.-C. Zha, "Numerical investigations of injection-slot-size effect on the performance of coflow jet airfoils," *Journal of Aircraft*, vol. 45, no. 6, pp. 2084–2091, 2008.

[28] Lefebvre, A. and Zha, G.-C. , "Design of High Wing Loading Compact Electric Airplane Utilizing Co-Flow Jet Flow Control." AIAA Paper 2015-0772, AIAA SciTech2015: 53nd Aerospace Sciences Meeting, Kissimmee, FL, 5-9 Jan 2015.

[29] Liu, Z.-X. and Zha, G.-C., "Transonic Airfoil Performance Enhancement Using Co-Flow Jet Active Flow Control." AIAA Paper 2016-3066, AIAA Aviation, Washington, D.C., June 13-17 2016.

[30] Lefebvre, A. and Zha, G.-C., "Trade Study of 3D Co-Flow Jet Wing for Cruise Performance." AIAA Paper 2016-0570, AIAA SCITECH2016, AIAA Aerospace Science Meeting, San Diego, CA, 4-8 January 2016.

[31] B. Wang and G.-C. Zha, "Detached-eddy simulation of a coflow jet airfoil at high angle of attack," *Journal of aircraft*, vol. 48, no. 5, pp. 1495–1502, 2011.

[32] Y. Yang and G. Zha, "Super-lift coefficient of active flow control airfoil: What is the limit?." AIAA Paper 2017-1693, AIAA SCITECH2017, 55th AIAA Aerospace Science Meeting, Grapevine, January 9-13 2017.

[33] Im, H.-S. and Zha, G.-C. and Dano, B. P. E., "Large Eddy Simulation of Coflow Jet Airfoil at High Angle of Attack," *Journal of Fluid Engineering, vol. 136(2), p. 021101*, 2014.

[34] D. Espinal, H.-S. Im, and G.-C. Zha, "Full-annulus simulation of nonsynchronous blade vibration excitation of an axial compressor," *Journal of Turbomachinery*, vol. 140, no. 3, 2018.

[35] H. Iim, X.-Y. Chen, and G. Zha, "Detached-eddy simulation of rotating stall inception for a full-annulus transonic rotor," *Journal of Propulsion and Power*, vol. 28, no. 4, pp. 782–798, 2012.

[36] S. A. Tran, D. A. Corson, and O. Sahni, "Synthetic jet based active flow control of dynamic stall phenomenon on wind turbines under yaw misalignment," in *32nd ASME Wind Energy Symposium*, p. 0871, 2014.

[37] A. L. Pape and J. Lecanu, "3d navier–stokes computations of a stall-regulated wind turbine," *Wind Energy: An International Journal for Progress and Applications in Wind Power Conversion Technology*, vol. 7, no. 4, pp. 309–324, 2004.